Dead-Time Compensation Based on a Modified Multiple Complex Coefficient Filter for Permanent Magnet Synchronous Machine Drives

Zheng Wu, Hengliang Zhang, Kai Liu, Wei Hua, *Senior Member, IEEE*, Gan Zhang, *Member, IEEE*, Bo Wang, Shichuan Ding, *Member, IEEE*, and Jun Hang

***Abstract*—In field-oriented vector control of permanent magnet synchronous machine (PMSM) drives, the dead time will cause the 5th and 7th current harmonics in the stationary reference frame. They are mapped to the negative and positive 6th harmonic current in the synchronous reference frame (SynRF), resulting in torque ripple and deterioration of control performance. To solve this problem, a new dead-time compensation method is proposed in this article. First, a multiple complex coefficient filter is modified with a low-pass filter being paralleled to extract positive and negative sequence components of 6th harmonic from *dq*-axes currents. Then, based on the extracted harmonics, a voltage feedback path with variable gains is designed in SynRF to eliminate the dead-time effect. Finally, the proposed method is implemented in a prototyped PMSM drive to verify its effectiveness. Both the simulations and experiments indicate that the proposed method can significantly weaken the dead-time effect with no additional hardware. Besides, it is also proved robust to the variable machine parameters.**

***Index Terms*—Dead-time compensation, inverter nonlinearity, low-pass filter (LPF), multiple complex coefficient filter (MCCF), permanent magnet synchronous machine (PMSM), vector control.**

I. Introduction

In RECENT years, pulsewidth modulation (PWM) voltage source inverter (VSI) has been widely used in motor-based adjustable speed drives. In the applications of PWM VSI, to prevent a short circuit of direct current (dc) link, a dead time is inserted in the period of PWM, where both the upper and lower switching devices are turned OFF. Unfavorably, the dead time will cause the output voltage error of the inverter, the distortion of armature currents, and the torque ripple, which severely affects the control performance of the drive system [1], [2]. Hence, the dead time should be compensated to weaken its adverse effects.

In previous literature, many compensation strategies have been studied. Most of them are based on the average value theory, where the average loss of volt seconds is first calculated, and then the action time of switching devices is compensated artificially depended on the polarity of phase current [3]–[10]. Although the implementation of such methods is simple, the polarity detection of phase current is a critical issue at the zero-crossing point due to the inevitable error and noise of the sampling circuit. To solve this problem, a freewheeling-current polarity detection circuit is designed to detect the phase current polarity accurately in [8], while a terminal voltage A/D conversion based current polarity detection method is presented in [10]. Although these methods achieve good performances, the additional circuits increase the cost and hardware complexity.

In order to avoid problems of current polarity detection, another method based on disturbance observation is studied in [11]–[15]. The disturbance observers are designed to identify the voltage error caused by the dead time in the synchronous reference frame (SynRF) and satisfied performances are achieved. Although the observer-based methods do not need additional hardware, they are sensitive to model parameters, and the observer gains tuning is complex.

Back to the effect of output voltage errors caused by the dead time, the 5th and 7th harmonics in phase current in the stationary reference frame (StaRF) are mapped to the 6th harmonic in SynRF. On this basis, alternative compensation strategies are studied in [16]–[21]. In [16], the 6th harmonic is subtracted from *dq*-axes reference currents. However, a small phase lag is caused by the PI regulator in the compensated voltage. Besides, a fixed gain in the feedback path should be adjusted when the operation condition changes. In order to solve these problems, the decomposer and compensator based on adaptive linear neuron (ADALINE) are designed in [20]. The compensated voltages are directly subtracted from reference voltages whilst the feedback gains are adjusted by the least mean square. However, apart from the rotor speed and *dq*-axes currents, the decomposer also needs the rotor angle and the phases of the harmonics in this method.

In this article, a new adaptive filter based compensation method is designed to suppress the dead-time effect by

Manuscript received January 16, 2021; revised April 9, 2021; accepted May 1, 2021. Date of publication May 7, 2021; date of current version July 30, 2021. This work was supported in part by the National Natural Science Foundation of China under Grant 51825701 and in part by the Key R&D Program of Jiangsu Province under Grant BE2020015. Recommended for publication by Associate Editor A. Muetze. *(Corresponding author: Wei Hua.)*

Zheng Wu, Hengliang Zhang, Kai Liu, Wei Hua, Gan Zhang, and Bo Wang are with the School of Electrical Engineering, Southeast University, Nanjing 210096, China (e-mail: wuzh_seu_207@163.com; zhanghengliang@seu.edu.cn; kliu@seu.edu.cn; huawei1978@seu.edu.cn; zhanggan@seu.edu.cn; b.wang@seu.edu.cn).

Shichuan Ding and Jun Hang are with the School of Electrical Engineering and Automation, Anhui University, Heifei 230601, China (e-mail: dingsc@126.com; jun_hang511@163.com).

Color versions of one or more figures in this article are available at https://doi.org/10.1109/TPEL.2021.3078167.

Digital Object Identifier 10.1109/TPEL.2021.3078167

minimizing the 6th harmonic in SynRF. The main characteristic of the proposed method is to utilize the positive and negative sequence components of 6th harmonics from *dq*-axes currents. Using the sequence information of 6th harmonic, the compensated voltage can be directly calculated by the voltage equation, which avoids the phase lag of PI current regulators in [16]. Besides, compared with [20], the way to obtain the harmonics needs no additional information, except the rotor speed and *dq*-axes currents. Moreover, the proposed method is robust to the motor parameters, comparing to the average theory based and disturbance observer based compensation methods, since a feedback path with variable gains is designed based on the magnitudes of the sequence harmonics.

In order to implement the proposed method, a proper adaptive filter is needed to obtain the sequence information of the *dq*-axes first. Many kinds of filters are investigated according to the literatures, including notch filter [22], moving average filter [23], multiple synchronous reference frame filter (MSRF) [24], multiple complex coefficient filter (MCCF) [25], second-order generalized integrator (SOGI) [26], delay signal cancellation [27], and repetitive controller [28]. Among them, only the MSRF, SOGI, and MCCF can extract positive and negative sequence components. However, the MSRF requires twice coordinate transformations and solving the trigonometric function of the rotor angle. The SOGI needs to deal with the second-order filter, leading to a heavy computational burden. Therefore, considering both the functions and computational burden, the MCCF is the most suitable technique.

The MCCF is first designed in StaRF [29], where the dc component cannot be handled. However, the dc component is the main composition of *dq*-axes currents, which means the original MCCF cannot be directly applied in SynRF. To eliminate the influence of the dc component, a low-pass filter (LPF) is added into the MCCF when processing the harmonics in *dq*-axes currents.

Based on the modified MCCF, a new dead-time compensation strategy is proposed in this article. In order to make the compensation method robust to the motor parameters, a feedback path with adaptive gains is designed.

The implementation of the proposed method is described as follows.

- *Step 1:* The negative and positive sequence components in *dq*-axes currents are extracted by the modified MCCF.
- *Step 2:* According to the amplitudes of the extracted harmonics, an adaptive strategy is designed to adjust two proportion feedback gains in *dq*-axes.
- *Step 3:* The amplitudes of feedback harmonic currents are adjusted by two variable proportion gains.
- *Step 4:* The voltage errors caused by the dead time are calculated by voltage equation by using positive and negative sequence components.
- *Step 5:* The voltage errors are subtracted from reference voltages to compensate the dead time.

The contributions of this article are listed as follows.

1) Both the positive and negative sequence components of 6th harmonic are used to compensate dead time.
2) The MCCF is modified to extract the positive and negative sequence components in SynRF.
3) A feedback path with adaptive gains is designed based on amplitudes of the positive and negative sequence components.

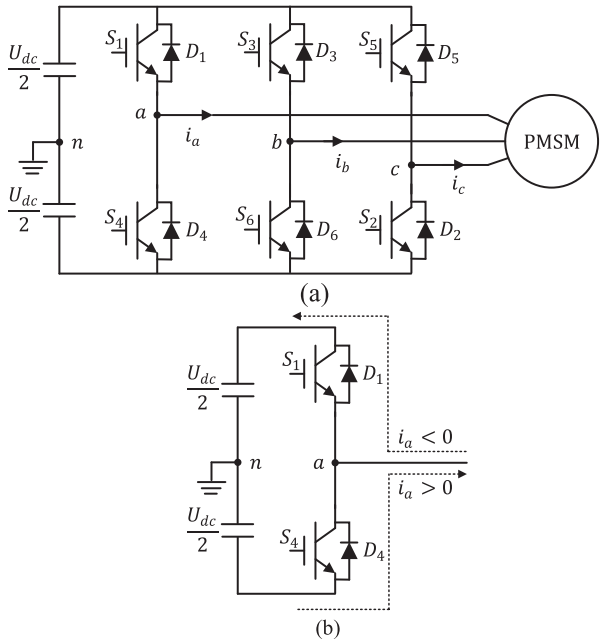

Fig. 1. PMSM-based drive system. (a) Three-phase PWM inverter with a PMSM load. (b) Current flow direction during the dead time in one phase leg.

The rest of this article is arranged as follows. The dead-time effects considering the inverter nonlinearity are analyzed in Section II. Then, the new compensation method is proposed in Section III. Further, verifications of both simulations and experiments are presented in Section IV. Finally, the conclusion is drawn in Section V.

II. Dead-Time Effects

The typical configuration of a VSI with a permanent magnet synchronous machine (PMSM) load is shown in Fig. 1(a), where insulated gate bipolar transistors (IGBTs) are used as switching devices. The current direction in one leg during dead time is defined as positive if the current flows from the inverter to the load, as shown in Fig. 1(b).

In Fig. 1(b), the switching device should be turned OFF when the other one is ON. However, the switching device cannot act instantaneously, resulting in that dc link is short-circuited when S_1 and S_2 act simultaneously. It is an extremely dangerous situation for the inverter, although its duration is short. Therefore, it is necessary to insert a dead time between the actions of two switch devices to avoid the short-circuit situation. During the dead time T_{dead}, both the two switching devices are turned OFF, and current flows through the free-wheeling diode D_1 or D_4 depending on the current polarity. Thus, the output voltage error of the inverter caused by the dead time is related to the polarity of

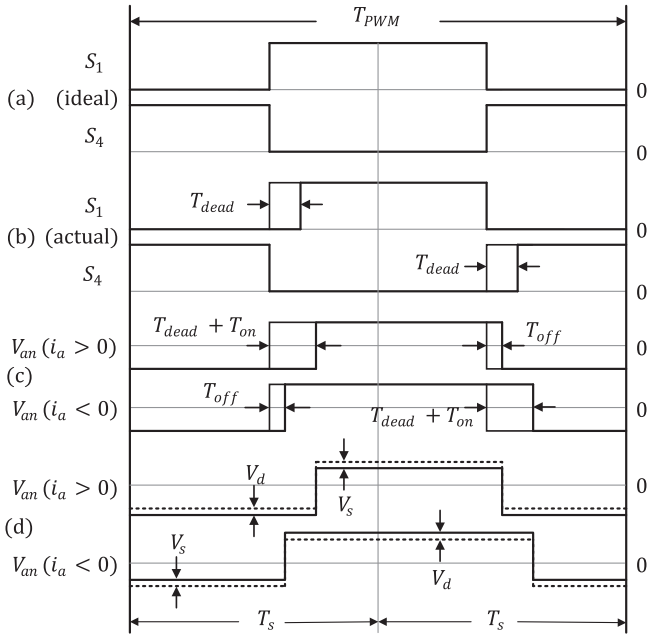

Fig. 2. Switching pattern and output phase voltages. (a) Ideal gating signals. (b) Actual gating signals. (c) Ideal phase output voltage. (d) Actual phase output voltage considering the dead time, turn ON/OFF time, and voltage drops.

phase current i_a. The zero-current clamping effects and the non-ideal characteristics, such as parasitic capacitance, in switching devices are not considered in this article. Thus, the switching pattern and the output phase voltage are shown in Fig. 2, where Fig. 2(a) and (b) indicates the ideal and the actual gating signals with and without the dead time, respectively. Further, Fig. 2(c) shows the phase output voltage V_{an} considering the dead time and the turn ON/OFF time. Then, the voltage drops are considered in Fig. 2(d).

The average voltage error in one PWM period yields

$$\Delta V_{an} = V_e * \text{sign}\,(i_a) \tag{1}$$

where

$$V_e = \frac{T_{\text{dead}} + T_{on} - T_{off}}{T_{\text{PWM}}}\ (V_{dc} - V_s + V_d) + \frac{V_s + V_d}{2} \tag{2}$$

$$\text{sign}\ (i_a) = \begin{cases} 1 & i_a > 0 \\ -1 & i_a < 0 \end{cases}$$

where T_{dead}, T_{on}, T_{off}, T_{pwm}, V_{dc}, V_s, and V_d represent the dead time, turn-ON/OFF time of switching device, PWM period, dc bus voltage, switching device conduction voltage drop, and forward voltage drop of freewheeling diode, respectively. Although the sum of V_s and V_d is relatively small, it cannot be ignored because of the volt drop in IGBT-based inverter, especially under low-speed and light-load operation.

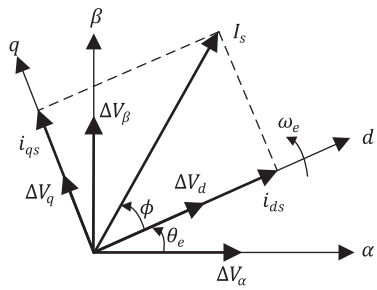

Fig. 3. Current vector and voltage errors in space.

Similarly, the average voltage errors of the other two legs (ΔV_{bn} and ΔV_{cn}) can be obtained by

$$\begin{cases} \Delta V_{bn} = V_e * \text{sign}\,(i_b) \\ \Delta V_{cn} = V_e * \text{sign}\,(i_c)\,. \end{cases} \tag{3}$$

Considering the phase winding connection is Y-type, the three-phase average voltage errors (ΔV_a, ΔV_b, and ΔV_c) yield

$$\begin{bmatrix} \Delta V_a \\ \Delta V_b \\ \Delta V_c \end{bmatrix} = \frac{1}{3} \begin{bmatrix} 2 & -1 & -1 \\ -1 & 2 & -1 \\ -1 & -1 & 2 \end{bmatrix} \begin{bmatrix} \Delta V_{an} \\ \Delta V_{bn} \\ \Delta V_{cn} \end{bmatrix}. \tag{4}$$

Further, the three-phase output voltage errors are transformed to StaRF as

$$\begin{bmatrix} \Delta V_\alpha \\ \Delta V_\beta \end{bmatrix} = \frac{2}{3} \begin{bmatrix} 1 & -\frac{1}{2} & -\frac{1}{2} \\ 0 & \frac{\sqrt{3}}{2} & -\frac{\sqrt{3}}{2} \end{bmatrix} \begin{bmatrix} \Delta V_a \\ \Delta V_b \\ \Delta V_c \end{bmatrix} \tag{5}$$

where ΔV_α/ΔV_β represents the average output voltage errors in StaRF, which can be further expanded into the Fourier series as

$$\begin{aligned} \Delta V_\alpha &= -\frac{4V_e}{\pi}\left\{\sin\gamma + \sum_{k=1}^{\infty}\left\{\frac{\sin(6k-1)\gamma}{6k-1} + \frac{\sin(6k+1)\gamma}{6k+1}\right\}\right\} \\ \Delta V_\beta &= \frac{4V_e}{\pi}\left\{\cos\gamma - \sum_{k=1}^{\infty}\left\{\frac{\cos(6k-1)\gamma}{6k-1} - \frac{\cos(6k+1)\gamma}{6k+1}\right\}\right\} \end{aligned} \tag{6}$$

where γ is the phase angle of current vector defined in Fig. 3 as

$$\gamma = \omega_e\, t + \phi - \pi/2,\ \phi = \tan^{-1}(i_{qs}/i_{ds})$$

where ω_e is the electrical speed.

Observing (6), it consists of the fundamental and the $6k\pm1$ orders of harmonics, which excludes the $3k$ and even orders of harmonics since the PMSM has three-phase windings and is half-wave symmetrical. Further, because the amplitudes of harmonics are small when $k\geq2$ [3], the subsequent analysis is aimed at the 5th and 7th harmonics.

Hence (6) is simplified as

$$\begin{aligned} \Delta V_\alpha &= -\frac{4V_e}{\pi}\left\{\sin\gamma + \frac{1}{5}\sin5\gamma + \frac{1}{7}\sin7\gamma\right\} \\ \Delta V_\beta &= \frac{4V_e}{\pi}\left\{\cos\gamma - \frac{1}{5}\cos5\gamma + \frac{1}{7}\cos7\gamma\right\}. \end{aligned} \tag{7}$$

By Park transformation, (7) is transformed into the SynRF as

$$\Delta V_d = \frac{4V_e}{\pi}\left\{\cos\phi + \frac{1}{5}\cos\left(-6\omega_e t - 5\phi\right) - \frac{1}{7}\cos\left(6\omega_e t + 7\phi\right)\right\}$$
$$\Delta V_q = \frac{4V_e}{\pi}\left\{\sin\phi + \frac{1}{5}\sin\left(-6\omega_e t - 5\phi\right) - \frac{1}{7}\sin\left(6\omega_e t + 7\phi\right)\right\}. \quad (8)$$

Applying (8) into PMSM, the resultant current harmonics in SynRF caused by the dead time and inverter nonlinearity can be defined as

$$\Delta I_d^{6th} = \frac{4V_e}{\pi}\left\{\frac{\cos\left(-6\omega_e t - 5\phi + \phi_s^{6th}\right)}{5Z_s^{6th}} - \frac{\cos\left(6\omega_e t + 7\phi - \phi_s^{6th}\right)}{7Z_s^{6th}}\right\}$$
$$\Delta I_q^{6th} = \frac{4V_e}{\pi}\left\{\frac{\sin\left(-6\omega_e t - 5\phi + \phi_s^{6th}\right)}{5Z_s^{6th}} - \frac{\sin\left(6\omega_e t + 7\phi - \phi_s^{6th}\right)}{7Z_s^{6th}}\right\} \quad (9)$$

where $Z_s^{6th} = \sqrt{R_s^2 + (6\omega_e L_s)^2}$, $\phi_d^{6th} = \tan^{-1}(6\omega_e L_s / R_s)$, and R_s and L_s are the stator resistance and the inductance per phase, respectively.

According to the polarity of frequency, the first item on the right side of (9) can be defined as the negative sequence component (I_d^- and I_q^-), while the second item is named as the positive sequence component ($I_d^+$and I_q^+). Therefore, the positive and negative sequence components in SynRF yield are expressed by

$$I_d^- = \frac{4V_e}{5\pi Z_s^{6th}}\cos\left(-6\omega_e t - 5\phi + \phi_s^{6th}\right)$$
$$I_d^+ = \frac{4V_e}{7\pi Z_s^{6th}}\cos\left(6\omega_e t + 7\phi - \phi_s^{6th}\right)$$
$$I_q^- = \frac{4V_e}{5\pi Z_s^{6th}}\sin\left(-6\omega_e t - 5\phi + \phi_s^{6th}\right)$$
$$I_q^+ = \frac{4V_e}{7\pi Z_s^{6th}}\sin\left(6\omega_e t + 7\phi - \phi_s^{6th}\right). \quad (10)$$

The voltage equation of a PMSM in SynRF is shown in (11), in which the current harmonics are ignored

$$\begin{cases} u_d = i_d R_s + p i_d L_s - \omega_e i_q L_s \\ u_q = i_q R_s + p i_q L_s + \omega_e i_d L_s + \omega_e \varphi_f \end{cases} \quad (11)$$

where p and φ_f is the Laplace operator and the PM flux-linkage, respectively.

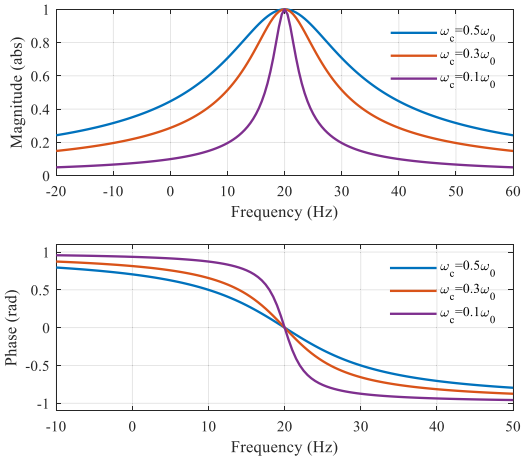

Fig. 4. Bode diagram of a first-order CCF with three different kc @$\omega 0 = 40\pi$ rad/s.

Substituting (10) into (11), the voltage errors due to current harmonics in SynRF can be obtained as (12). If the current harmonic sequences in (10) are identified, the error of output voltage can be calculated by (12) as well. Then, the voltage errors could be removed from the reference voltage

$$u_{de} = \left(i_d^+ + i_d^-\right) R_s + 5\omega_e L_s i_q^- - 7\omega_e L_s i_q^+$$
$$u_{qe} = \left(i_q^+ + i_q^-\right) R_s - 5\omega_e L_s i_d^- + 7\omega_e L_s i_d^+. \quad (12)$$

III. Dead-Time Compensation Strategy

According to the analysis in Section II, the key aspect of the proposed compensation strategy is to extract the negative and positive sequence components from phase currents in SynRF. Thus, the MCCF is chosen in this article, considering the characteristics and the computation burden of filters.

A. Modified MCCF

An ideal first-order complex coefficient filter (CCF) has the unit gain and zero phase shift at selected frequency, while attenuating the signals at other frequencies.

The expression of a CCF in s-domain yields

$$\text{CCF (s)} = \frac{\omega_c}{s - j\omega_0 + \omega_c} \quad (13)$$

where ω_c, ω_0, and j is the bandwidth of CCF, selected angular frequency of CCF, and the sign of complex number, respectively.

Here, ω_c is set as $k_c\omega_0$, where k_c is a proportion coefficient. The Bode diagram of a CCF is shown in Fig. 4, where $\omega_0 = 40\pi$ rad/s with three different values of k_c, namely, 0.5, 0.3, and 0.1. From Fig. 4, the CCF features a higher attenuation at a nonselected frequency and a better ability to extract specific frequency when k_c is smaller, which is also demonstrated in the attenuation rate (AR) formula (14). Meanwhile, the response of CCF is slower with a smaller k_c, according to the pole locus of

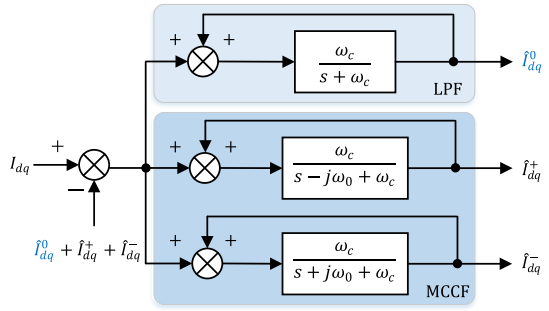

Fig. 5. Scheme of a modified MCCF parallel with a LPF.

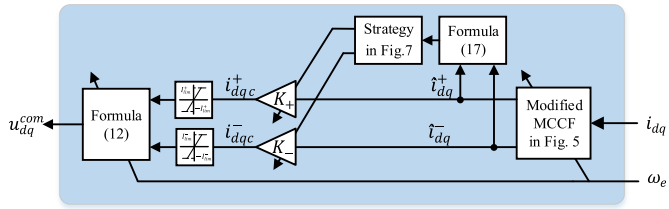

Fig. 6. Block diagram of proposed dead-time compensation.

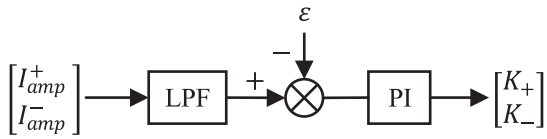

Fig. 7. Compensation gains dynamic recognition strategy.

CCF in (15)

$$\mathrm{AR}\left(j\omega\right) = \frac{k_c\omega_0}{\sqrt{\left(\omega-\omega_0\right)^2+\left(k_c\omega_0\right)^2}} \tag{14}$$

$$p = -k_c\omega_0 + j\omega_0. \tag{15}$$

The structure of MCCF was first proposed to extract the specific sequences of voltage in [29]. It is composed of multiple CCFs with different selected frequencies in parallel. Different from the voltage of grid-connected converter in the StaRF which contains only the negative and positive sequences, the current of PMSM-load inverter in the SynRF contains dc component as the dominant one. From Fig. 4, although the AR at 0 Hz is small, the magnitude of the dc component in the SynRF is too large to decay to a small value. Therefore, the MCCF in [29] cannot be directly applied in this article.

A modified MCCF with an LPF being paralleled is shown in Fig. 5, where $I^*_{dq} = I^*_d + jI^*_q$ ($*$ on behalf of $+$, $-$ and 0), and I_{dq}, $\hat{I}^0_{dq}$, $\hat{I}^+_{dq}$, and $\hat{I}^-_{dq}$ are sampling currents, extracted dc components, extracted positive, and negative sequence components in SynRF. Due to the dc components extracted by the LPF are subtracted from every path in the MCCF, the ability of the MCCF to suppress the dc component is enhanced. Besides, when applying the modified MCCF, the ω_0 is set as 6 ω_e. Then, the $-$6th and $+$6th harmonics can be obtained in outputs signals ($\hat{I}^+_{dq}$ and $\hat{I}^-_{dq}$).

The frequency-domain equation of the modified MCCF can be derived as detailed in Appendix. The solution to the time-domain equation (A4) indicates that the modified MCCF can accurately extract the dc component, the positive sequences, and the negative sequence components of input signals.

B. Proposed Dead-Time Compensation Method

The block diagram of the proposed dead-time compensation strategy is shown in Fig. 6. With the help of the modified MCCF, the positive sequence components ($\hat{i}^+_{dq}$) and negative sequence components ($\hat{i}^-_{dq}$) can be extracted from the currents in SynRF (i_{dq}). Then, the voltage errors resulting from the dead time and inverter nonlinearity can be calculated by (12). The effectiveness of the proposed compensation method depends on the detected harmonic current amplitudes, which will decrease when the compensation method is applied. Therefore, two proportion gains (K_+ and K_-) are proposed to change the estimated harmonic currents shown as

$$\begin{bmatrix} i^+_{dqc} \\ i^-_{dqc} \end{bmatrix} = \begin{bmatrix} K_+ \\ K_- \end{bmatrix}^T \begin{bmatrix} \hat{i}^+_{dq} \\ \hat{i}^-_{dq} \end{bmatrix}. \tag{16}$$

C. Dynamic Recognition of Feedback Gains

As mentioned above, K_+ and K_- are designed to increase the amplitudes of extracted harmonic currents. A similar gain which is a fixed value is applied in [16]. However, when the operation state of the motor changes, the feedback gains need to be modified to maintain the compensation effect [20]. Therefore, a dynamic recognition strategy for the feedback gains is designed, shown in Fig. 6.

From (10), it can be seen that the same sequence components in dq-axes feature the same amplitude, frequency, and phase, ideally. Thus, the amplitudes of the extracted positive and negative sequences components (I^+_{amp} and I^-_{amp}) are obtained by mathematical calculation as

$$\begin{bmatrix} I^+_{\mathrm{amp}} \\ I^-_{\mathrm{amp}} \end{bmatrix} = \begin{bmatrix} \sqrt{\hat{i}^{+2}_d + \hat{i}^{+2}_q} \\ \sqrt{\hat{i}^{-2}_d + \hat{i}^{-2}_q} \end{bmatrix}. \tag{17}$$

In fact, the calculated amplitudes are fluctuating, resulting from the current sampling noise and the filter discretization. In order to address this issue, an LPF is used, as shown in Fig. 7. Then, a PI regulator is used to modify the feedback gains as

$$\begin{bmatrix} K_+ \\ K_- \end{bmatrix} = \frac{\omega_{LPF}}{s+\omega_{LPF}} \left(k_p + \frac{k_i}{s}\right) \begin{bmatrix} I^+_{\mathrm{amp}} \\ I^-_{\mathrm{amp}} \end{bmatrix} \tag{18}$$

where ω_{LPF}, k_p, and k_i are the cutoff frequency of the LPF, proportion, and integral gains of the PI, respectively. Since the values of amplitude are always non-negative, the feedback coefficients increase progressively when the reference of PI (ε) is set as zero. In order to solve this problem, the reference value ε is recommended to set as a positive value, which can represent the

TABLE I
KEY SPECIFICATIONS AND PARAMETERS OF THE PMSM

Item	Value	Item	Value
Rate Speed	3000rpm	Stator phase resistance	0.96Ω
Rated power	3kW	Stator phase inductance	166.5uH
Rated current	18.6A	Pole-pairs number	4

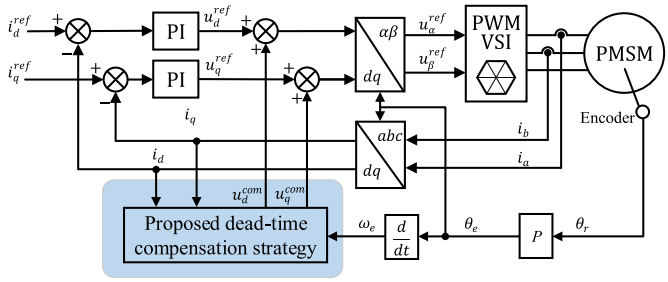

Fig. 8. Block diagram of a PMSM driver system with the proposed dead-time compensation strategy.

expected value of the harmonics. It is recommending to set ε as 0.02% of the rate current of motor, according to the experimental experience.

In this compensation scheme, the rotor speed is required in the application of modified MCCF. If the incorrect rotor speed is given, the incorrect positive and negative sequence components might be obtained. This results in the wrong compensation voltage supplied to the motor, which might lead to the system instability. In order to mitigate the impact of this situation, the saturation functions are used to limit the compensation currents shown in Fig. 6. The limits are experimentally obtained as peak values of the positive and negative sequence components in (17). In addition, although this scheme uses the motor parameters to calculate the compensation voltages as shown in (12), the variable feedback gains can counteract the effect of parameter uncertainty.

IV. SIMULATIONS AND EXPERIMENTS

In order to verify the effectiveness of the proposed dead-time compensation strategy, both the simulations and experiments are carried out in this section. The key parameters of the PMSM used in this paper are given in Table I.

A. Simulation Results

A control model considering the effect of the dead time and inverter nonlinearity is built in MATLAB/Simulink. Fig. 8 shows the control block diagram with PI current regulators and the proposed dead-time compensation strategy. In the simulation, both the sampling frequency and PWM switching frequency are set as 10 kHz, while the dead time is 2 μs. The key specifications of the simulation system are listed in Table II.

The current waveforms without the dead-time compensation strategy are illustrated in Fig. 9. It is found that there are obvious distortions appearing in the peaks, valleys, and zero-crossing points in the current waveform of phase A (top one), compared

TABLE II
SPECIFICATIONS AND PARAMETERS UNDER SIMULATION AND EXPERIMENT

Description	Value	Description	Value
DC link voltage	200V	Switching device	IGBT
PWM	10kHz	Turn-on time	0.13-0.15μs
Dead time	2μs	Turn-off time	0.3-0.4μs

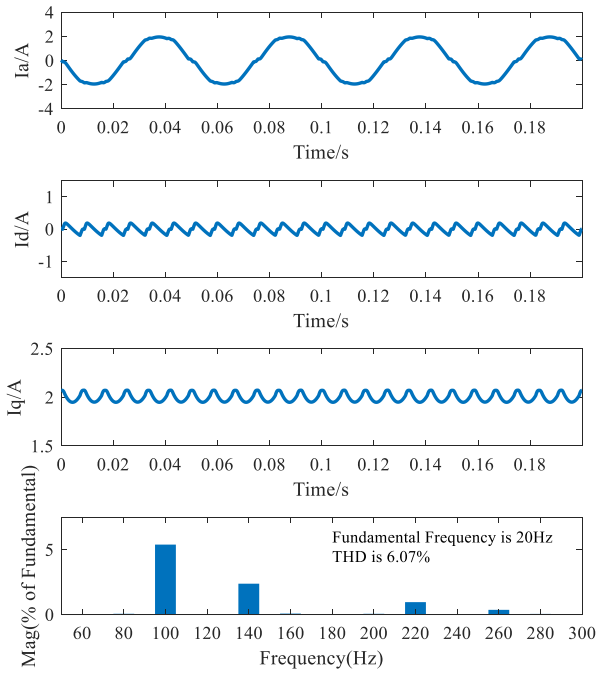

Fig. 9. Simulation results without the compensation method for the PMSM at 300 r/min. From top to bottom: phase A current, d-axis current, q-axis current, and spectrum of phase A current.

with a standard sinewave. Besides, both dq-axes currents exhibit considerable fluctuations. The corresponding current spectrum of phase A is presented at bottom of Fig. 9, which demonstrates that the 5th and 7th components are the dominant harmonics. The simulation results agree well with the theoretical analysis in Section II.

In contrast, Fig. 10 shows the current waveforms with the proposed dead-time compensation strategy under the same conditions. From Fig. 10, the current waveform of phase A has been significantly improved, whilst the fluctuations of dq-axes currents are remarkably reduced compared with Fig. 9. Moreover, the spectrum of phase A current in Fig. 10 indicates that the original 5th and 7th current harmonics of phase A are efficiently decreased compared with that in Fig. 9. Although the 11th and 13th harmonics increase slightly, the compensation effect is not influenced by this phenomenon. Because the decreases of 5th and 7th harmonics are much greater than the increases of 11th and 13th harmonics, the resultant current THD of phase A current is reduced from 6.07% to 2.18%. Therefore, the effectiveness of the compensation method can be verified by the above-mentioned simulations.

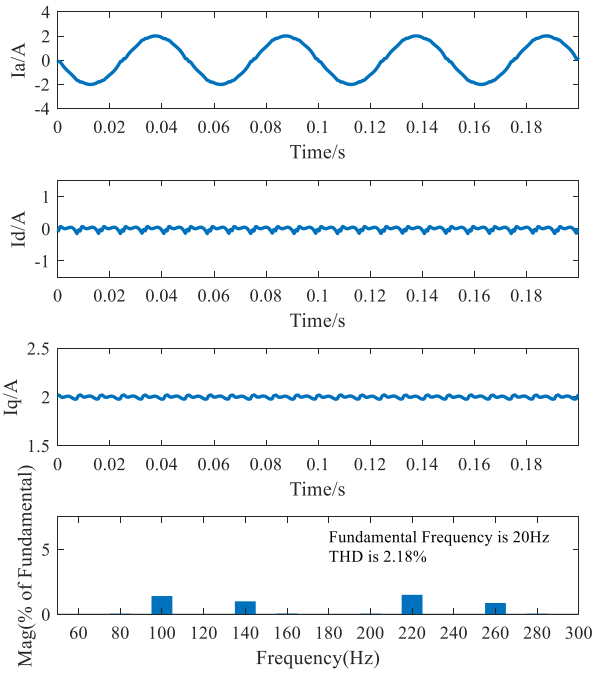

Fig. 10. Simulation results with the compensation method for the PMSM at 300 r/min. From top to bottom: phase A current, *d*-axis current, *q*-axis current and spectrum of phase A current.

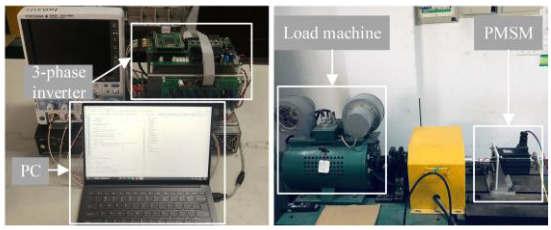

Fig. 11. Experimental setup for a PMSM.

B. Experimental Results

The experimental platform consists of a PMSM, three-phase VSI, PC, and induction motor driven by an ABB-ACS800 as a load, shown as Fig. 11. The experiments are carried out under several conditions, including steady state, transient state, and uncertain motor parameters state. The sampling frequency and the PWM frequency are both set as 10 kHz. The proportion coefficient k_c of MCCF is set to 0.01. The bandwidth of the current regulator is set as 1500 rad/s. Besides, k_p and k_i of the PI regulator in Fig. 7 are set as 100 and 60, respectively. The experimental results are presented in Figs. 12–16.

The experimental results without and with the compensation strategy under steady state (the motor speed is 300 r/min) are shown in Figs. 12 and 13, respectively. Two parts are contained in figures of the oscilloscope. The upper ones are the integral waveforms, and the waveforms inside the red rectangle are enlarged in the nether ones. In Fig. 12(a), the current waveform of phase A is deteriorated by the dead time and inverter nonlinearity. The corresponding *dq*-axes currents exhibit obvious fluctuations, especially for I_d. The current spectrum of phase A presented

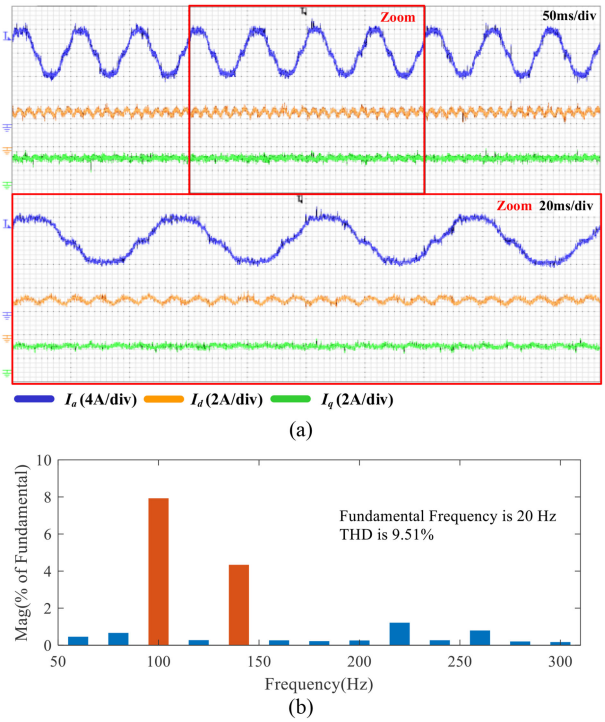

Fig. 12. Experiment results without the compensation strategy for the PMSM at 300 r/min. (a) Current waveforms. (b) Current spectrum of phase A.

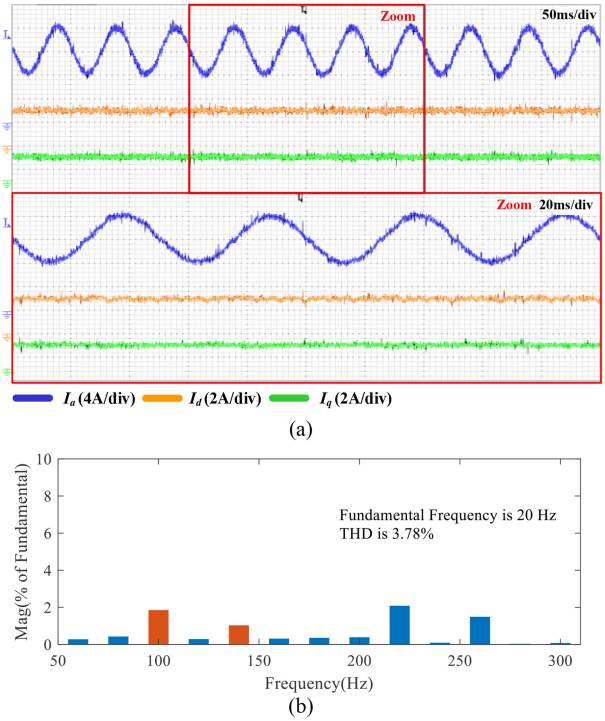

Fig. 13. Experiment results with the proposed method for the PMSM at 300 r/min. (a) Current waveforms. (b) Current spectrum of phase A.

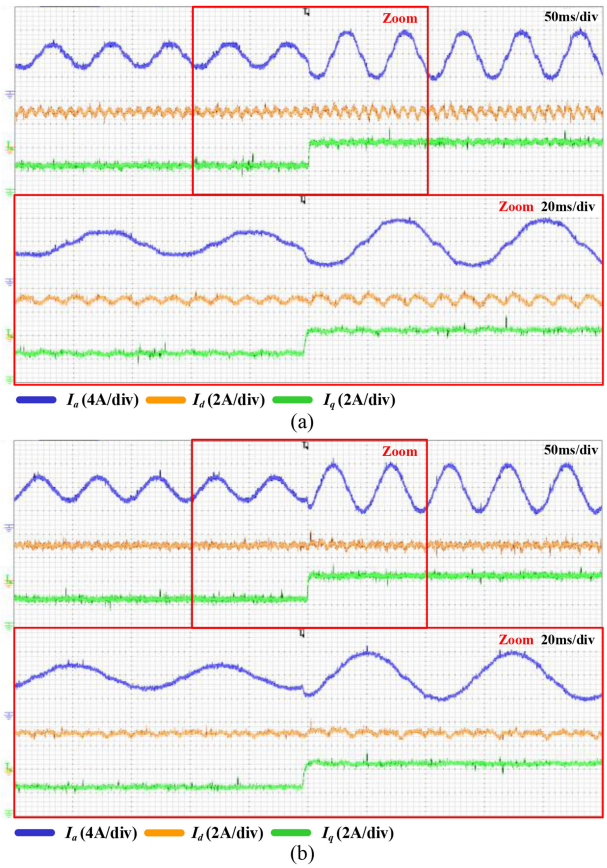

Fig. 14. Experimental current waveforms under transient on-load state. (a) Without compensation strategy. (b) With composed strategy.

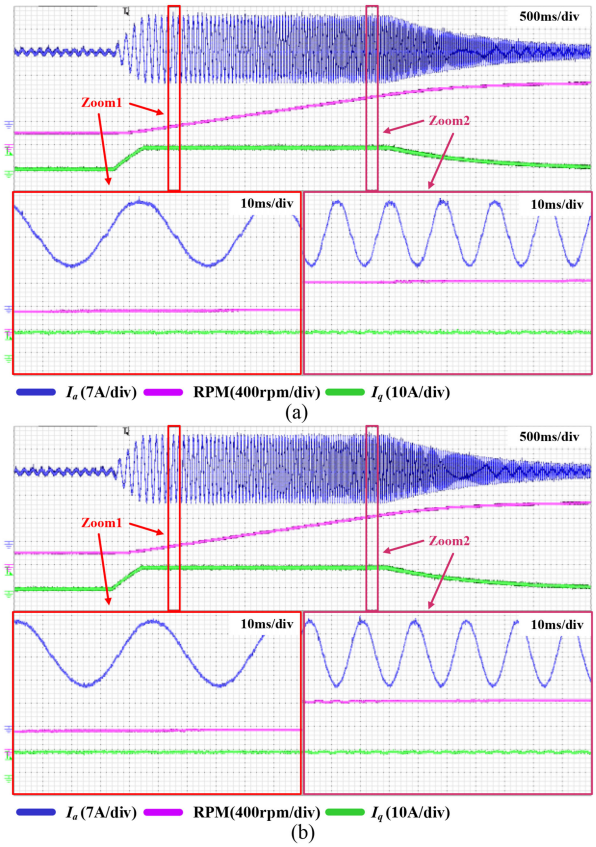

Fig. 15. Experimental current waveforms under transient varying speed state. (a) Without compensation strategy (b) With compensation strategy.

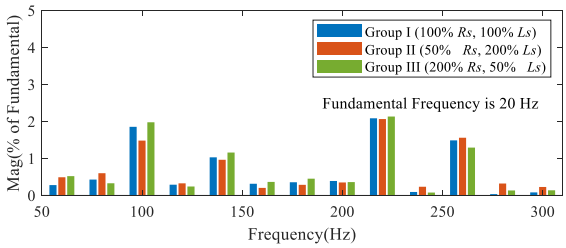

Fig. 16. Experimental current waveforms under uncertain motor parameters.

in Fig. 12(b) demonstrates that the 5th and 7th harmonics are dominant as marked in orange. In Fig. 13, the experimental results by the proposed compensation method are displayed. It is found that the current waveform distortion of phase A and the fluctuations of d- and q-axis currents are significantly decreased as shown in Fig. 13(a). Besides, the current magnitudes of the 5th and 7th harmonics of phase A after compensation are effectively reduced as shown in Fig. 13(b). Even the 11th and 13th harmonics rise slightly, the total current THD of phase A is declined from 9.51% to 3.78%.

For the case of the transient q-axis current experiment, the measured results are shown in Fig. 14. The transient moments of the upper ones are enlarged below, as shown in Fig. 14. The motor is initially operated at 300 r/min with a q-axis current of 2 A, and then the q-axis reference current is suddenly changed to 4 A. Comparing Fig. 14(a) and (b), the proposed method does not deteriorate the response of the current loop, and it features a good suppression effect on the harmonics caused by dead time.

Fig. 15 demonstrates the experimental results under transient varying speed operation, where the PMSM initially operates at 200 r/min, and then the reference speed jumps to 1000 r/min. Due to the large rotational inertia of the load motor system, it took some time to accelerate to 1000 r/min. Two different stages of the acceleration process are enlarged, shown in "Zoom1" and "Zoom2". Comparing the current waveforms in Fig. 15(a) and (b), the proposed strategy can compensate the dead time and inverter nonlinearity well without any degradation to the speed transient performance of the control system.

Finally, to verify the robustness of the proposed dead-time compensation method to the variable motor parameters, three groups of comparative experiments with different phase resistance (R_s) and winding inductance (L_s) are carried out, namely, Group I (100% of R_s and 100% of L_s), Group II (50% of R_s and 200% of L_s), and Group III (200% of R_s and 50% of L_s). The motor speed is set as 300 r/min and the load torque is 0.8 N·m. Fig. 16 displays the currents spectra of phase A of these three groups with different motor parameters. From Fig. 16, the current harmonics distributions are almost the same, validating the robustness of the proposed compensation strategy.

V. Conclusion

In this article, a new dead-time compensation strategy based on the sequence components of 6th current harmonic is proposed for PMSM drives. First, the impact of dead time on drive systems is analyzed. Based on the analysis, the voltage errors caused by dead time can be obtained by the positive and negative sequence components of the 6th harmonic. Then, an MCCF parallel with an LPF is designed to extra the positive and negative sequence components of *dq*-axes currents. Finally, a harmonic feedback path with variable gains is designed to suppress the dead-time effect based on the amplitudes of sequence components. The effectiveness and robustness of the proposed dead-time compensation strategy are verified by both the simulations and experiments on a prototyped PMSM drive system.

Appendix

The modified MCCF structure, shown in Fig. 5, is expressed in the frequency domain as

$$\begin{aligned}
\hat{I}_d^0\ (s) &= \tfrac{\omega_c}{s+\omega_c}\left[I_d\,(s) - \hat{I}_d^+\,(s) - \hat{I}_d^-\,(s)\right]\\
\hat{I}_q^0\ (s) &= \tfrac{\omega_c}{s+\omega_c}\left[I_q\,(s) - \hat{I}_q^+\,(s) - \hat{I}_q^-\,(s)\right]\\
\hat{I}_d^+\ (s) &= \tfrac{\omega_c}{s-j\omega_0+\omega_c}\left[I_d\,(s) - \hat{I}_d^0\,(s) - \hat{I}_d^-\,(s)\right]\\
\hat{I}_q^+\ (s) &= \tfrac{\omega_c}{s-j\omega_0+\omega_c}\left[I_q\,(s) - \hat{I}_q^0\,(s) - \hat{I}_q^-\,(s)\right]\\
\hat{I}_d^-\ (s) &= \tfrac{\omega_c}{s+j\omega_0+\omega_c}\left[I_d\,(s) - \hat{I}_d^0\,(s) - \hat{I}_d^+\,(s)\right]\\
\hat{I}_q^-\ (s) &= \tfrac{\omega_c}{s+j\omega_0+\omega_c}\left[I_q\,(s) - \hat{I}_q^0\,(s) - \hat{I}_q^+\,(s)\right].
\end{aligned} \tag{A1}$$

The corresponding time-domain equation can be derived from (A1) as

$$\begin{cases} \dot{x}\ (t) = A\,(t)\cdot x\,(t) + B\,(t)\cdot i\,(t) \\ y\ (t) = C\cdot x\,(t) \end{cases} \tag{A2}$$

where

$$x\ (t) = y\,(t) = \left[\hat{I}_d^0\,(t)\ \hat{I}_q^0\,(t)\ \hat{I}_d^+\,(t)\ \hat{I}_q^+\,(t)\ \hat{I}_d^-\,(t)\ \hat{I}_q^-\,(t)\right]^T$$

$$i\ (t) = [I_d\ I_q\ I_d\ I_q\ I_d\ I_q]^T$$

$$A\ (t) = \begin{bmatrix} -\omega_c & 0 & -\omega_c & 0 & -\omega_c & 0 \\ 0 & -\omega_c & 0 & -\omega_c & 0 & -\omega_c \\ -\omega_c & 0 & -\omega_c & -\omega_0 & -\omega_c & 0 \\ 0 & -\omega_c & \omega_0 & -\omega_c & 0 & -\omega_c \\ -\omega_c & 0 & -\omega_c & 0 & -\omega_c & \omega_0 \\ 0 & -\omega_c & 0 & -\omega_c & -\omega_0 & -\omega_c \end{bmatrix}$$

$$B\ (t) = \omega_c\ \cdot E_{6*4}$$

$$\mathrm{C}\ (\mathrm{t}) = E_{6*6}$$

where E_{6*4} and E_{6*6} are diagonal matrices with values of 1 along the diagonal.

The solution to (A2) can be obtained as

$$x\ (t) = e^{A(t-t_0)}\,x\,(t_0) + \int_{t_0}^{t} e^{A(t-\tau)}Bu\,(\tau)\,d\tau. \tag{A3}$$

According to the deduction in [22], the solution expression can be obtained as

$$\begin{aligned} x\ (t) &= \left[\hat{I}_d^0\,(t)\ \hat{I}_q^0\,(t)\ \hat{I}_d^+\,(t)\ \hat{I}_q^+\,(t)\ \hat{I}_d^-\,(t)\ \hat{I}_q^-\,(t)\right]^T \\ &= \left[I_d^0\,(t)\ I_q^0\,(t)\ I_d^+\,(t)\ I_q^+\,(t)\ I_d^-\,(t)\ I_q^-\,(t)\right]^T. \end{aligned} \tag{A4}$$

References

[1] A. Guha and G. Narayanan, "Impact of dead time on inverter input current, DC-Link dynamics, and light-load instability in rectifier-inverter-fed induction motor drives," *IEEE Trans. Ind. Appl.*, vol. 54, no. 2, pp. 1414–1424, Mar./Apr. 2018.

[2] A. Guha and G. Narayanan, "Impact of undercompensation and overcompensation of dead-time effect on small-signal stability of induction motor drive," *IEEE Trans. Ind. Appl.*, vol. 54, no. 6, pp. 6027–6041, Nov./Dec. 2018.

[3] Z. Shen and D. Jiang, "Dead-Time effect compensation method based on current ripple prediction for voltage-source inverters," *IEEE Trans. Power Electron.*, vol. 34, no. 1, pp. 971–983, Jan. 2019.

[4] D. Wang, M. Wang, Y. Shen, Q. Li, and X. Liang, "Online feedback dead time compensation strategy for three-level T-Type inverters," *IEEE Trans. Ind. Electron.*, vol. 67, no. 9, pp. 7260–7268, Sep. 2020.

[5] J.-H. Lee and S.-K. Sul AE, "Inverter nonlinearity compensation through dead time effect estimation," *IEEE Trans. Power Electron.*, to be published, doi: 10.1109/TPEL.2021.3061285.

[6] N. Diao, X. Sun, C. Song, Q. Zhang, and Z. Zhang, "A Multi-modulation times SVPWM for dead time effect elimination in three-level neutral point clamped converters," *IEEE Trans. Ind. Electron.*, vol. 68, no. 7, pp. 5476–5485, Jul. 2021.

[7] L. Guo, N. Jin, C. Gan, L. Xu, and Q. Wang, "An improved model predictive control strategy to reduce common-mode voltage for two-level voltage source inverters considering dead-time effects," *IEEE Trans. Ind. Electron.*, vol. 66, no. 5, pp. 3561–3572, May 2019.

[8] Y. Lin and Y. Lai, "Dead-time elimination of PWM-Controlled inverter/converter without separate power sources for current polarity detection circuit," *IEEE Trans. Ind. Electron.*, vol. 56, no. 6, pp. 2121–2127, Jun. 2009.

[9] A. Lewicki, "Dead-time effect compensation based on additional phase current measurements," *IEEE Trans. Ind. Electron.*, vol. 62, no. 7, pp. 4078–4085, Jul. 2015.

[10] G. Liu, D. Wang, Y. Jin, M. Wang, and P. Zhang, "Current-detection-independent dead-time compensation method based on terminal voltage A/D conversion for PWM VSI," *IEEE Trans. Ind. Electron.*, vol. 64, no. 10, pp. 7689–7699, Oct. 2017.

[11] X. Zhang, Y. Cheng, Z. Zhao, and K. Yan, "Optimized model predictive control with dead-time voltage vector for PMSM drives," *IEEE Trans. Power Electron.*, vol. 36, no. 3, pp. 3149–3158, Mar. 2021.

[12] Z. Zhang, H. Lu, D. J. Costinett, F. Wang, L. M. Tolbert, and B. J. Blalock, "Model-based dead time optimization for voltage-source converters utilizing silicon carbide semiconductors," *IEEE Trans. Power Electron.*, vol. 32, no. 11, pp. 8833–8844, Nov. 2017.

[13] N. Bedetti, S. Calligaro, and R. Petrella, "Self-commissioning of inverter dead-time compensation by multiple linear regression based on a physical model," *IEEE Trans. Ind. Appl.*, vol. 51, no. 5, pp. 3954–3964, Sep. 2015.

[14] N. Bedetti, S. Calligaro, and R. Petrella, "Self-commissioning of inverter dead-time compensation by multiple linear regression based on a physical model," *IEEE Trans. Ind. Appl.*, vol. 51, no. 5, pp. 3954–3964, Sep. 2015.

[15] K. Liu and Z. Q. Zhu, "Online estimation of the rotor flux linkage and voltage-source inverter nonlinearity in permanent magnet synchronous machine drives," *IEEE Trans. Power Electron.*, vol. 29, no. 1, pp. 418–427, Jan. 2014.

[16] S.-Y. Kim and S.-Y. Park, "Compensation of dead-time effects based on adaptive harmonic filtering in the vector-controlled AC motor drives," *IEEE Trans. Ind. Electron.*, vol. 54, no. 3, pp. 1768–1777, Jun. 2007.

[17] Z. Wu, K. Ding, Z. Yang, and G. He, "Analytical prediction and minimization of dead-time related harmonics in PMSM," *IEEE Trans. Power Electron.*, to be published, doi: 10.1109/TIE.2020.3014583.

[18] Z. Tang and B. Akin, "Suppression of dead-time distortion through revised repetitive controller in PMSM drives," *IEEE Trans. Energy Convers.*, vol. 32, no. 3, pp. 918–930, Sep. 2017.
[19] G. Liu, B. Chen, K. Wang, and X. Song, "Selective current harmonic suppression for high-speed PMSM based on high-precision harmonic detection method," *IEEE Trans. Ind. Informat.*, vol. 15, no. 6, pp. 3457–3468, Jun. 2019.
[20] T. Qiu, X. Wen, and F. Zhao, "Adaptive-linear-neuron-based dead-time effects compensation scheme for PMSM drives," *IEEE Trans. Power Electron.*, vol. 31, no. 3, pp. 2530–2538, Mar. 2016.
[21] Z. Tang and B. Akin, "A new LMS algorithm based deadtime compensation method for PMSM FOC drives," *IEEE Trans. Ind. Appl.*, vol. 54, no. 6, pp. 6472–6484, Nov./Dec. 2018.
[22] E. Rodriguez-Diaz, F. D. Freijedo, J. C. Vasquez, and J. M. Guerrero, "Analysis and comparison of notch filter and capacitor voltage feedforward active damping techniques for LCL grid-connected converters," *IEEE Trans. Power Electron.*, vol. 34, no. 4, pp. 3958–3972, Apr. 2019.
[23] J. Liu, E. Isufi, and G. Leus, "Filter design for autoregressive moving average graph filters," *IEEE Trans. Signal Inf. Process. Netw.*, vol. 5, no. 1, pp. 47–60, Mar. 2019.
[24] E. Uz-Logoglu, O. Salor, and M. Ermis, "Online characterization of interharmonics and harmonics of AC electric arc furnaces by multiple synchronous reference frame analysis," *IEEE Trans. Ind. Appl.*, vol. 52, no. 3, pp. 2673–2683, May/Jun. 2016.
[25] Y. Terriche, S. Golestan, J. M. Guerrero, and J. C. Vasquez, "Multiple-complex coefficient-filter-based PLL for improving the performance of shunt active power filter under adverse grid conditions," in *Proc. IEEE Power Energy Soc. Gen. Meeting*, 2018, pp. 1–5.
[26] C. M. Hackl and M. Landerer, "Modified second-order generalized integrators with modified frequency locked loop for fast harmonics estimation of distorted single-phase signals," *IEEE Trans. Power Electron.*, vol. 35, no. 3, pp. 3298–3309, Mar. 2020.
[27] S. Golestan, J. M. Guerrero, J. C. Vasquez, A. M. Abusorrah, and Y. Al-Turki, "Research on variable-length transfer delay and delayed-signal-cancellation-based PLLs," *IEEE Trans. Power Electron.*, vol. 33, no. 10, pp. 8388–8398, Oct. 2018.
[28] R. C. Neto, F. A. S. Neves, and H. E. P. de Souza, "Complex nk + m repetitive controller applied to space vectors: Advantages and stability analysis," *IEEE Trans. Power Electron.*, vol. 36, no. 3, pp. 3573–3590, Mar. 2021.
[29] X. Guo, W. Wu, and Z. Chen, "Multiple-complex coefficient-filter-based phase-locked loop and synchronization technique for three-phase grid-interfaced converters in distributed utility networks," *IEEE Trans. Ind. Electron.*, vol. 58, no. 4, pp. 1194–1204, Apr. 2011.

Zheng Wu received the B.Sc. degree in electrical engineering in 2018 from the School of Electrical Engineering, Southeast University, Nanjing, China, where he is currently working toward the Ph.D. degree in electrical engineering.

His research interests include high-speed electric machine drives and sensorless control technology.

Hengliang Zhang was born in Anhui, China, in 1992. He received the B.Sc. and Ph.D. degrees in electrical engineering from Southeast University, Nanjing, China, in 2014 and 2020, respectively.

From 2018 to 2019, he was with the Power Electronics, Machines and Control Group, The University of Nottingham, Nottingham, U.K., as a Joint-Supervised Ph.D. Student. He is currently with Southeast University, as a Lecturer. His research interests include the design and analysis of permanent magnet machines in electric vehicles and servo systems.

Kai Liu received the B.Sc., M.Sc., and Ph.D. degrees in electrical engineering from the Harbin Institute of Technology, Harbin, China, in 2005, 2007, and 2014, respectively.

Since 2015, he has been with Southeast University, where he is currently a Lecturer with the School of Electrical Engineering. His teaching and research interests include control of electrical machines and flywheel energy storage systems.

Wei Hua (Senior Member, IEEE) received the B.Sc. and Ph.D. degrees in electrical engineering from Southeast University, Nanjing, China, in 2001 and 2007, respectively.

From 2004 to 2005, he was with the Department of Electronics and Electrical Engineering, The University of Sheffield, U.K., as a Joint-Supervised Ph.D. Student. Since 2007, he has been with Southeast University, where he is currently a Chief Professor and a Distinguished Professor of Jiangsu Province. He has coauthored more than 150 technical papers. He holds 50 patents in his areas of interest, which include design, analysis, and control of electrical machines, especially for PM brushless machines and switching reluctance machines, etc.

Gan Zhang (Member, IEEE) received the B.Sc. and Ph.D. degrees in electrical engineering from the School of Electrical Engineering, Southeast University, Nanjing, China, in 2011 and 2016, respectively.

From January 2015 to February 2016, he was a Joint Ph.D. Student with the Department of Energy Technology, Aalborg University, Aalborg, Denmark. Since 2016, he has been with Southeast University, where he is currently a Lecturer with the School of Electrical Engineering. His teaching and research interests include the design and analysis of novel permanent-magnet brushless electrical machines, and electric vehicle technology.

Bo Wang (Member, IEEE) received the B.Eng. and M.Sc. degrees in electrical engineering from the Nanjing University of Aeronautics and Astronautics, Nanjing, China, in 2009 and 2012, respectively, and the Ph.D. degree in electronic and electrical engineering from the University of Sheffield, Sheffield, U.K., in 2018.

From 2012 to 2014, he was a Senior Engineer with Delta Electronics Company Ltd., Nanjing, China. From 2017 to 2018, he was a Research Associate with the Department of Electronic and Electrical Engineering, University of Sheffield. In 2018, he joined the School of Electrical Engineering, Southeast University, as an Associate Research Fellow. In 2020, he joined Hong Kong PolyU under the Hong Kong Scholar Program. His research interests include the permanent-magnet machine drives, electric traction, and fault tolerant systems.

Shichuan Ding (Member, IEEE) received the B.Sc. degree in automation from Anhui University, Hefei, China, in 2001, the M.Sc. degree from University of Science and Technology of China, Hefei, China, in 2006, and the Ph.D. degree in electrical engineering from Southeast University, Nanjing, China, in 2018.

Since 2001, he has been with Anhui University, where he is currently a Professor. From April 2015 to April 2016, he was a Research Scholar with Wisconsin Electric Machines and Power Electronics Consortium, University of Wisconsin Madison. In recent years, he has authored and coauthored more than 40 technical papers. His research interests include electrical machine drive, electrical machine fault diagnosis and fault tolerant control, power electronics applications, and energy management in EVs, in industrial application and in power system.

Jun Hang (Member, IEEE) received the B.Sc. and M.Sc. degrees in electrical engineering from the Anhui University of Science and Technology, Huainan, China, in 2008 and 2011, respectively, and the Ph.D. degree in electrical engineering from Southeast University, Nanjing, China, in 2016.

From April 2015 to July 2015, He was a Joint Ph.D. Student with the Department of Energy Technology, Aalborg University, Denmark. Since 2016, he has been with Anhui University, Hefei, China, where he is currently an Associate Professor with the School of Electrical Engineering and Automation. In recent years, he has authored and coauthored more than 30 technical papers. His current research interests include condition monitoring, fault diagnosis, permanent-magnet machine and renewable energy.

Dr. Hang was the recipient of the First Prize of 2016 Student Thesis Contest (Ph.D. Category), IEEE Industry Applications Society.